Two-Stage Motion Correction for Super-Resolution Ultrasound Imaging in Human Lower Limb

Sevan Harput, Kirsten Christensen-Jeffries, Jemma Brown, Yuanwei Li, Katherine J. Williams, Alun H. Davies, Robert J. Eckersley, Christopher Dunsby, and Meng-Xing Tang

***Abstract*— The structure of microvasculature cannot be resolved using conventional ultrasound (US) imaging due to the fundamental diffraction limit at clinical US frequencies. It is possible to overcome this resolution limitation by localizing individual microbubbles through multiple frames and forming a superresolved image, which usually requires seconds to minutes of acquisition. Over this time interval, motion is inevitable and tissue movement is typically a combination of large- and small-scale tissue translation and deformation. Therefore, super-resolution (SR) imaging is prone to motion artifacts as other imaging modalities based on multiple acquisitions are. This paper investigates the feasibility of a two-stage motion estimation method, which is a combination of affine and nonrigid estimation, for SR US imaging. First, the motion correction accuracy of the proposed method is evaluated using simulations with increasing complexity of motion. A mean absolute error of 12.2 μm was achieved in simulations for the worst-case scenario. The motion correction algorithm was then applied to a clinical data set to demonstrate its potential to enable *in vivo* SR US imaging in the presence of patient motion. The size of the identified microvessels from the clinical SR images was measured to assess the feasibility of the two-stage motion correction method, which reduced the width of the motion-blurred microvessels to approximately 1.5-fold.**

***Index Terms*— Motion correction, motion estimation, non-rigid motion, super-localization, super-resolution imaging.**

Manuscript received November 8, 2017; accepted March 28, 2018. Date of publication April 9, 2018; date of current version May 7, 2018. This work was supported in part by the EPSRC under Grant EP/N015487/1 and Grant EP/N014855/1, in part by the King's College London and Imperial College London EPSRC Centre for Doctoral Training in Medical Imaging under Grant EP/L015226/1, in part by the Wellcome EPSRC Centre for Medical Engineering at King's College London under Grant WT 203148/Z/16/Z, in part by the Department of Health through the National Institute for Health Research Comprehensive Biomedical Research Center Award to Guy's and St Thomas' NHS Foundation Trust in partnership with the King's College London and King's College Hospital NHS Foundation Trust, and in part by the Graham–Dixon Foundation. *(Robert J. Eckersley, Christopher Dunsby, and Meng-Xing Tang contributed equally to this work.) (Corresponding author: Sevan Harput.)*

S. Harput, Y. Li, and M.-X. Tang are with the Ultrasound Laboratory for Imaging and Sensing Group, Department of Bioengineering, Imperial College London, London SW7 2AZ, U.K. (e-mail: s.harput@imperial.ac.uk; yuanwei.li09@imperial.ac.uk; mengxing.tang@imperial.ac.uk).

K. Christensen-Jeffries, J. Brown, and R. J. Eckersley are with the Division of Imaging Sciences, Biomedical Engineering Department, King's College London, London SE1 7EH, U.K. (e-mail: kirsten.christensen-jeffries@kcl.ac.uk; jemma.brown@kcl.ac.uk; robert.eckersley@kcl.ac.uk).

K. J. Williams and A. H. Davies are with the Section of Surgery, Imperial College London, Charing Cross Hospital, London W6 8RF, U.K. (e-mail: k.williams@imperial.ac.uk, and a.h.davies@imperial.ac.uk).

C. Dunsby is with the Department of Physics and the Centre for Pathology, Imperial College London, London SW7 2AZ, U.K. (e-mail: christopher.dunsby@imperial.ac.uk).

Digital Object Identifier 10.1109/TUFFC.2018.2824846

I. Introduction

Among the many medical imaging modalities, ultrasound (US) imaging stands out in terms of accessibility and cost. Using conventional B-mode or contrast-enhanced US (CEUS) imaging at clinical frequencies, subwavelength structures, such as the microvasculature, cannot be resolved due to the fundamental diffraction limit. This limit can, however, be overcome by the method of US super-resolution (SR) techniques, such as US localization microscopy [1], where the final image is formed by localizing spatially isolated microbubbles (MBs) through multiple acquired frames. Viessmann *et al.* [2] demonstrated that it is possible to spatially resolve two touching 200-μm internal diameter tubes using an unmodified clinical CEUS system operating 2 MHz. Since then, several research groups have demonstrated the use of SR imaging within microfluidic channels [3], a tissue phantom with microvessels through an *ex vivo* human skull [4], and *in vivo* in mouse and rat models [5]–[9]. A theoretical localization precision as low as 1.8 μm was predicted for ultrasonic localization microscopy for human breast imaging at 7 MHz [10].

In vivo imaging introduces the additional complexity of sample motion during image acquisition. Christensen-Jeffries *et al.* [5] mapped the microvasculature *in vivo* in a mouse ear where vessel features as fine as 19 μm, which is approximately 6$\times$ smaller than the receive wavelength ($\sim\lambda_{rx}/6$), were visualized in under 10 min of US acquisition using an unmodified clinical system. In this paper, a 2-D subpixel cross correlation was used for motion correction and gating to avoid artifacts due to motion caused by breathing. Errico *et al.* [6] imaged an *in vivo* rat brain that was fixed within a stereotactic frame to minimize the motion. A 10-min acquisition was required for each coronal plane of the whole-brain scan to form the SR images that can resolve two vessels located 16 μm ($\sim\lambda_{rx}/6$) apart. In their later study, Hingot *et al.* [11] used a cross correlation-based method to correct the motion between frames, which was applied within a block of 200 images acquired at 500 frames/s. Ackermann and Schmitz [7] performed multiple MB tracking *in vivo* in a tumor xenograft-bearing mouse and measured capillary blood flow (<1 mm/s). Due to respiratory motion, they discarded 1151 frames out of 6000 frames acquired over 4 min. Lin *et al.* [8] detected vessels *in vivo* in tumor-bearing rats as small as 25 μm ($\sim\lambda_{rx}/7$) by 3-D US localization microscopy with a total acquisition time of 11.5 min (16 s for

each 2-D slice). They excluded 20%–30% of the acquired frames due to the breathing induced motion artifacts to avoid the interference of bubble positions.

Rather than gating or stabilizing the sample, another approach to reducing motion artifacts is to use a higher concentration of MBs and shorter acquisition times to form SR images; however, the final resolution of SR images obtained via localization of spatially nonisolated MBs is currently poorer than those obtained using the methods described earlier. Bar-Zion *et al.* [9] imaged *in vivo* rabbit kidney and tumor models using higher order statistics by acquiring less than a second of high frame rate US data. They achieved an improvement of 50% in spatial resolution with a significantly shorter acquisition time as low as 0.1 s that makes the proposed approach clinically applicable. However, even at this short time scale, SR images will still be prone to motion artifacts at the micrometer level and motion correction may be required, especially for handheld clinical scans.

For SR US imaging to become useful clinically, motion artifacts must be addressed first. During normal breathing, the diaphragm moves 15 mm and the chest circumference changes 7 mm, and respiration causes translation of organs in the upper body [12]. Although respiratory motion is usually considered to be rigid, human soft tissue is mostly anisotropic and tissue deformation is only in the linear elastic region of the stress–strain curve for tissue strains up to 5% [13]. Cardiac motion is very complex and nonrigid, involving longitudinal and radial contractions. Although it does not generate as much motion as respiration, the region of the liver adjacent to the heart is typically displaced by approximately 4 mm [12]. Moreover, there are many unpredictable and unavoidable sources of motion in the body generating rigid and nonrigid motion such as swallowing, coughing, peristalsis, bowel movements, pulsations of arterioles and venules, and other local muscle movements. Motion is an inherent part of diagnostic imaging and, unless corrected, it sets the achievable resolution limit in SR US imaging.

Doppler-based motion estimation is sensitive to small phase delays in the RF data and it can compensate for the local motion in the axial (or equivalently the radial) direction. Poree *et al.* [14] achieved contrast and image quality improvement by applying this technique to high frame rate echocardiography. Doppler-based motion estimation worked well for this application since the lateral motion observed in their study was smaller than half of the lateral (or equivalently the cross-range) resolution. Gammelmark and Jensen [15] demonstrated that the axial motion compensation alone is not sufficient when the total motion in lateral direction is large in comparison to the wavelength. They have performed the motion correction by tracking the position of the pixels in each low-resolution image acquired with the synthetic transmit aperture method, which is similar to SR imaging in a way that a combination of many low-resolution images is necessary to generate a high-resolution image.

Ideally, the motion should be compensated with an accuracy higher than the spatial resolution to be achieved in the SR image. When the problem of motion correction is solved for clinical US imaging, it will be possible to achieve a resolution below 10 μm, which will enable the imaging of human capillary vessels that may benefit many applications. Imaging blood vessels at microscale can reveal the elements that modulate endothelial barrier function, such as blood–brain barrier opening [16]. Many features of the immune system's interactions with small blood vessels and microcirculatory networks can be observed by using SR imaging. Vascular abnormalities associated with tumor growth can be monitored in detail, where the acoustic angiography using contrast agents already revealed the potential of using high-resolution imaging [17]. High-resolution and accurate imaging is the key to success for the diagnosis and endovascular treatment of peripheral arterial disease [18].

In this paper, a *two-stage* motion estimation algorithm previously used in magnetic resonance imaging was applied to SR US imaging [19], with the goal of correcting for both rigid and nonrigid sample motion. The accuracy of the motion estimation method was analyzed *in silico* and also the application of this method to clinical SR imaging was demonstrated *in vivo*.

II. Motion Estimation and Correction

Here, we refer to motion as the combination of US probe motion and tissue motion such as respiratory motion, cardiac motion, and other patient movements. It is not usually possible to control these sources of motion, which can be on the order of millimeters for an *in vivo* SR image that requires seconds to minutes of data acquisition. In SR imaging, motion can be as low as a micrometer for high frame rate imaging (>1000 frames/s). However, the total acquisition time is determined by the speed of the physiological processes, such as the blood flow velocity in microvessels, not by the imaging frame rate [5], [20]. Over such a long duration, the motion between the first and the last frame will be a combination of rigid motion and local nonrigid deformations with different amplitudes.

A. Two-Stage Motion Estimation

The motion estimation is based on an image registration approach, which was previously applied to the MRI and the MATLAB (The MathWorks, Natick, MA, USA) codes is currently available to download [21]. This approach is based on the work of Rueckert *et al.* [22] and Lee *et al.* [23] and it is capable of performing *rigid*, *affine*, *nonrigid*, and *two-stage* motion estimation. The *rigid* registration is capable of capturing the translation and rotation. The *affine* registration can estimate translation, rotation, shearing, and resizing. The *nonrigid* registration is a B-spline-based free-form deformation that can estimate the local compression and rarefaction of tissue [22]. *Nonrigid* registration is achieved by minimizing a cost function, which is a combination of the cost associated with the smoothness of the transformation and the cost associated with the image similarity. Smoothness of the transformation is crucial to mimic the local deformation of the soft tissue, where adjacent points move cohesively. Smoothness is achieved by introducing a penalty term $C_{\text{regularization}}(T)$, which regularizes the transformation and ensures that the resultant

transformation field is not noisy. In summary, a high value of the regularization parameter ensures neighboring transformation points are similar and that they vary smoothly over space. A low value allows greater freedom of changes in neighboring transformation points. It is hard to relate this term to an actual physical quantity or fit a model to predict the optimal value; therefore, this paper used a grid search method to determine an appropriate value of $C_{\text{regularization}}(T)$. When the registration algorithm finishes optimizing the cost function for a given $C_{\text{regularization}}(T)$ and converges, the transformation matrix T saves the estimation result that can be used to correct the motion in the registered frames. *Two-stage* image registration is a combination of *affine* registration that estimates the global motion, and *nonrigid* registration that can estimate the local deformation of tissue.

For a small regularization penalty, motion estimation results in a viscous fluidlike registration with long computational time where pixels can move almost independently, which is not realistic for human soft tissue. For a large regularization penalty, registration finishes after a small number of iterations and can result in large errors for complex motion fields, such as combinations of large global movement and small local deformations. The *two-stage* registration approach is advantageous because the *affine* registration finds a rough global estimate first and then the *nonrigid* registration refines the final solution. The two-step approach effectively increases the range over which the *nonrigid* registration will work and improves the speed and the convergence of the optimization process.

There is an obvious tradeoff between the resolution of the mesh size used in the registration model and computational complexity. In order to achieve the best compromise between the resolution or the accuracy of the nonrigid deformation and the computational cost, this model implements a hierarchical multiresolution approach [23]. Resolution of the control grid spacing is increased along with the image resolution from a coarse to a fine level and several iterations are performed at each stage until the cost function is minimized [22].

B. Application of Motion Correction to Super-Resolution

Fig. 1 shows the SR image processing chain. Motion estimation was performed as the first step on the B-mode image and the transformation matrix was used to correct the motion in the CEUS images. *Two-stage* registration implicitly performs *affine* and *nonrigid* registrations and outputs one transformation matrix and the motion corrected image.

For the clinical study, the CEUS images were generated by the clinical US system. After the motion correction stage, a spatio-temporal filtering based on singular value decomposition was applied to remove the residual tissue echoes from the CEUS images [24]. Separation of MB and tissue signals is crucial for SR imaging and it is not a straightforward procedure since nonlinear propagation of US through MB contrast agents can lead to imaging artifacts including subsequent erroneous localization of MBs [25], [26]. After the filtering stage, a threshold was applied to remove the noise before MB detection. In the MB detection stage, an intensity threshold was used to reject large signals, which might be due to multiple MBs. Finally, the super-localization stage was performed as explained in [27].

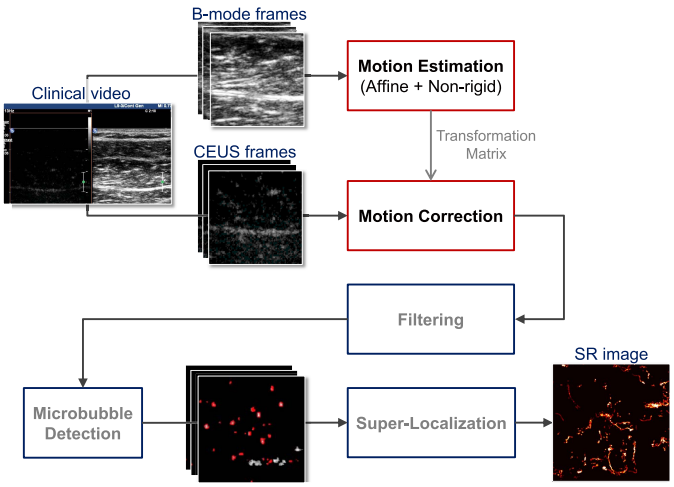

Fig. 1. Processing chain of SR imaging. *Affine* and *nonrigid* motion estimation are the first two steps of the process.

III. Materials and Methods

A. Simulation Study

To verify the accuracy of the proposed motion estimation method, Field II simulations were performed [28], [29]. Controlled motion patterns were simulated on a tissue phantom with increasing complexity of motion as shown in Figs. 2–4. In all simulations, white Gaussian noise was added to the simulated data before the beamforming operation and the SNR was calculated as a ratio between mean tissue signal and standard deviation of the white Gaussian noise.

Probe motion was simulated by moving the location of scatterers together in the axial or lateral direction as shown in Fig. 2. Translation of scatterers in the axial or lateral direction creates a rigid tissue motion with uniform displacement. These simulations were performed for 11 different exponentially spaced motion amplitudes for a range of 1–1024 μm and they were repeated 20 times with each repeat having a different noise.

Tissue deformation was generated by displacing the scattering points as a function of depth or lateral distance using a linear stress–strain relation to mimic the effect compression from top by an US probe or compression from side by a moving organ or muscle. By moving scatterers independent of each other, a nonrigid tissue motion was created, as shown in Fig. 3 (left) and (middle). As shown in Fig. 3 (right), the motion within the imaging field changes from a few micrometers to up to a millimeter, which corresponds to a maximum of 2% compression in the axial direction and 2.5% compression in the lateral direction.

For the last simulation, a more realistic motion pattern was simulated in Field II by using the motion field estimated from a clinical scan. Two frames acquired approximately 10 s apart were chosen as the reference frame and the frame

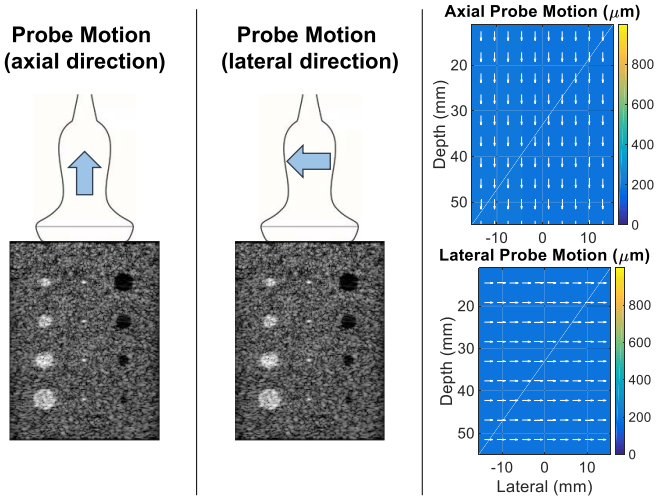

Fig. 2. Simulated probe motion in axial (left) and lateral (middle) directions. By moving the probe away from the center of the tissue phantom, a rigid motion is generated. Right: tissue motion direction with arrows and the colorbar represents the motion amplitude for both cases. Probe motion was simulated for a motion range of 1–1024 μm, but only 256-μm motion is shown here for clarity.

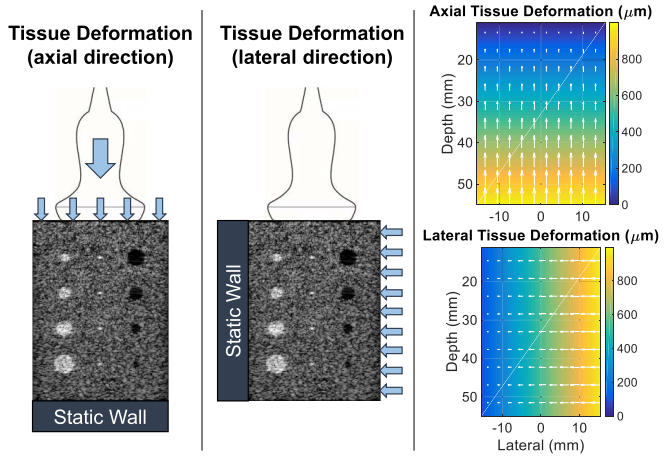

Fig. 3. Simulated tissue deformations in the axial (left) and lateral (middle) directions. A nonrigid motion is generated to mimic tissue deformation caused by probe compression or muscle contraction. Right: tissue motion direction with arrows and the colorbar represents the motion amplitude for both cases. Tissue deformation was simulated for a wide range of values, but only 2% and 2.5% compression in the axial and lateral directions are shown here for clarity.

with motion. The extracted motion field from these two frames accommodates a combination of a large scale counterclockwise motion located at the south–east of the image and a small scale clockwise motion located at the north–west of the image with an average motion of 203 ± 113 μm as shown in Fig. 4 (middle). This motion field was then applied to a numerical simulation of a homogeneous tissue phantom shown in Fig. 4 (left).

Simulation parameters were chosen specifically to match the parameters of the clinical study with a center frequency 6 MHz, 80% bandwidth, 160 elements, and a pitch of 237.5 μm. The -6-dB width of the point spread function at 25-mm depth was 287 and 397 μm in the axial and lateral directions, respectively.

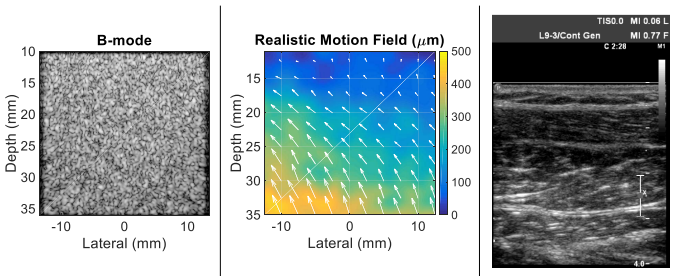

Fig. 4. Left: simulated realistic motion in Field II on a homogeneous tissue phantom without any dominant structures. Middle: Extracted motion field from a clinical data set that was subsequently applied on the homogeneous phantom shown on the left to simulate a realistic motion. The colorbar represents the motion amplitude in micrometers and the white arrows show the direction of the tissue motion. Right: Example B-mode frame acquired with a commercial US scanner that was used to extract a realistic motion.

The simulated tissue phantom had 10 scatterers per resolution cell for every simulation to generate a fully developed speckle pattern [30]. For the simulations with probe motion and tissue deformations, the phantom included circular hypoechoic and hyperechoic regions with a diameter of 2, 3, 4, and 5 mm and 4-point scatterers (Figs. 2 and 3). For the realistic motion simulations (Fig. 4), a homogeneous phantom was used without any structure, which makes the motion estimation harder, because in this case, there are no dominant features in the B-mode frames to aid the motion estimation, and the motion estimation is, therefore, obtained purely from the simulated speckle pattern. The attenuation coefficient was set to 0.5 dB/cm/MHz and white Gaussian noise was added to the simulated data before beamforming. By shifting the scatterers together or independently, a different speckle pattern was generated for all tested scenarios. The signal to noise ratio in the simulated B-mode image was varied between 20 dB, which is the empirical lower bound where a suitable motion correction is possible for SR imaging with the proposed approach, and 50 dB, which is the dynamic range of the US scanner used in the clinical study.

The motion estimation algorithm was applied to the simulated B-mode image after envelope detection, log-compression, and downsampling. The resulting images had a pixel size of 60×60 μm^2 and a 50-dB dynamic range. During image registration, most of the parameters were kept the same except the grid spacing and the regularization penalty, which had a large effect on motion estimation accuracy for some cases. The similarity measure of squared pixel distance (also called squared difference) was used for all estimations. Among two interpolation techniques available with this motion estimation method, linear interpolation was used instead of cubic, as cubic interpolation was found to have higher error values due to the discontinuities inside and at the boundaries of the image [31]. The final result was cubic interpolated. The registration was always initialized with a uniform grid and the maximum number of grid refinement steps used by the multiresolution method was fixed to two. The registration method was changed between *rigid*, *affine*, *nonrigid*, and *two-stage* (also referred to as *both* inside the MATLAB code) in order to demonstrate the accuracy of each method for

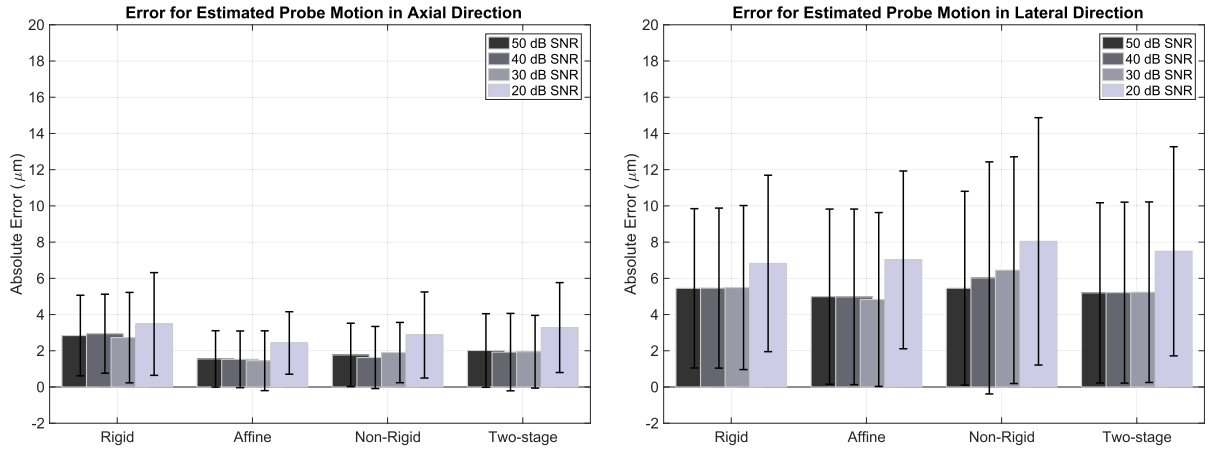

Fig. 5. Results of simulations carried out with rigid sample translation (also referred to as probe motion) as shown in Fig. 2. The average absolute motion estimation error for all simulated motion values (11 simulations spanning 1–1024 μm, each repeated 20 times) are shown for the axial (left) and lateral (right) directions, respectively. Error bars show the standard deviation in absolute motion estimation error over all simulated motion values. Values are shown for SNR values of 50, 40, 30, and 20 dB for all motion estimation methods.

different scenarios. A grid spacing of 128×128 was used for all simulations except the simulated translational motion, where a larger spacing of 256×256 and 512×512 showed an improvement. When a grid size of 128×128 was chosen initially, the registration function also used a 64×64 grid and a 32×32 grid thanks to two subsequent grid refinement steps. To demonstrate the potential of the motion estimation method, the regularization of the *two-stage* and *nonrigid* registrations were optimized for each simulation. Each simulation was run for a set of regularization values ($10^{-6} \leq C_{\text{regularization}}(T) \geq 1$) and the penalty parameter that achieved the minimum error was chosen as the optimum value. For the simulated probe motion, lowest error values were achieved by using a higher regularization parameter as opposed to the cases for simulated tissue deformation and realistic motion.

B. Clinical Study

Healthy volunteers were recruited from a research center (Charing Cross Hospital, Imperial College London, London, U.K.). The study was approved by the National Research and Ethics Committee (Reference 13/LO/0943), and each participant provided written informed consent.

Clinical data was acquired in the tibialis anterior muscle using a Philips iU22 US scanner (Philips Medical Systems, Bothell, WA, USA) with a handheld 3–9-MHz linear array probe. A vial of Sonovue (Bracco S.p.A, Milan, Italy) was diluted using normal saline (25 mg in 20 mL) and was administered as an intravenous infusion (VueJect, Bracco S.p.A, Milan, Italy) at a rate of 4 mL/min via an 18G cannula placed in an antecubital vein. The cannula was flushed with saline [5 mL of sodium chloride 9 mg/mL (0.9%) solution] and disconnected. B-mode and CEUS (power modulation) frames were acquired using the RS imaging mode of the Philips scanner operating around a 6-MHz center frequency with a mechanical index of 0.06 and a dynamic range of 50 dB.

Several acquisitions from three healthy volunteers were recorded over a duration of 40–55 s with 500–700 B-mode and CEUS frames at a frame rate of 13 Hz and the resulting data was saved to disk as video files. Supplementary video shows the *in vivo* CEUS and B-mode data. It can be seen that the tissue signal dominates the B-mode images and that the moving bubble signals will not significantly affect the motion estimation. B-mode frames were used for motion estimation and the motion correction was performed on CEUS frames before formation of the SR images.

IV. Results

A. Simulation Study

The accuracy of the motion estimation for the simulated probe motion in the axial and lateral directions are given in Fig. 5 (left) and (right), respectively. The mean absolute error values are plotted with an error bar that represents the standard deviation for a range of motion between 1 and 1024 μm.

In the case of rigid probe motion in the axial direction, all methods estimated the motion with less than 3.5-μm absolute error and with a standard deviation smaller than 3 μm. In the case of rigid probe motion in the lateral direction, the absolute error increased for all motion estimation methods, where *nonrigid* motion estimation gave larger error values (8 ± 7 μm) for the simulations with 20-dB SNR.

Results of the nonrigid tissue deformation simulations are shown in Fig. 6 (left) and (right) for all motion estimation methods. Results of the *rigid* motion estimation for all noise levels were above 45 μm, which is not suitable for SR US imaging. Both *affine* and *two-stage* motion estimation performed similarly for tissue deformation shown in Fig. 3 with absolute error values below 5.4 ± 5.2 μm for lateral and below 3.7 ± 2.9 μm for axial motion. Due to the nature of the simulated linear elastic compression of tissue, *affine* motion estimation performed better than the *nonrigid* motion estimation.

The computation time including both the motion estimation and motion correction were measured for an image with a size

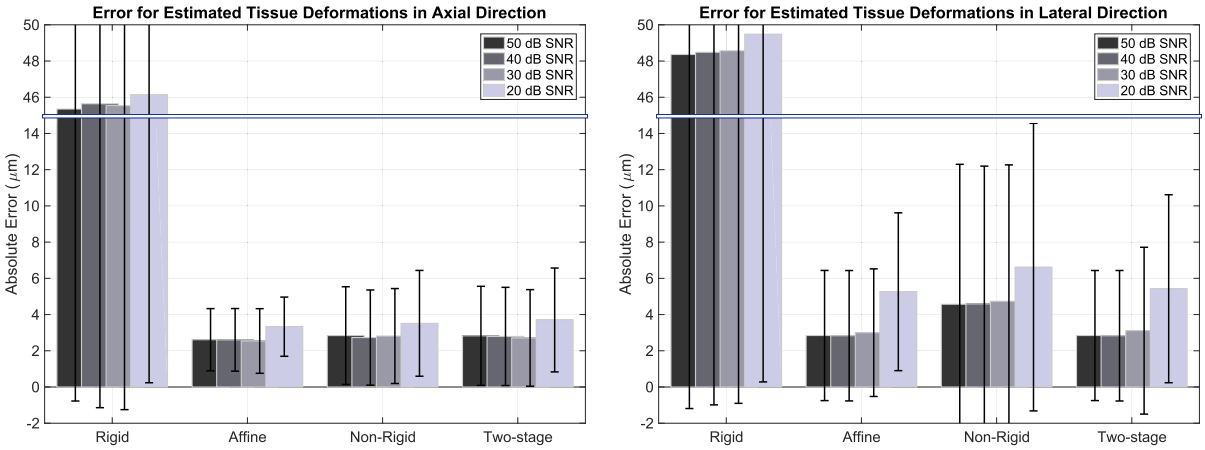

Fig. 6. Results of simulations carried out with nonrigid sample deformation (also referred to as tissue deformation) as shown in Fig. 3. The average absolute motion estimation error for all simulated motion values (11 pairs of simulations with a compression ratio of 0.002%–2% in the axial direction and 0.0025%–2.5% in the lateral direction, each repeated 20 times) are shown for the axial (left) and lateral (right) directions, respectively. Error bars show the standard deviation in absolute motion estimation error over all simulated motion values. Values are shown for SNR values of 50, 40, 30, and 20 dB for all motion estimation methods.

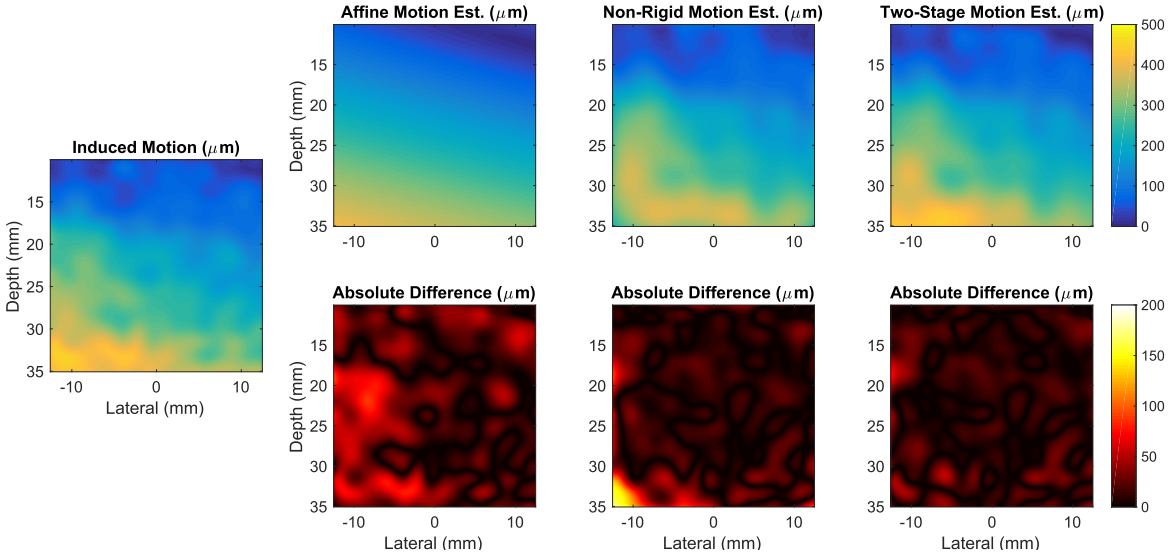

Fig. 7. Left: Simulated motion field applied on the B-mode image as shown in Fig. 4. Top: motion estimated with *affine*, *nonrigid*, and *two-stage* registration methods for the simulated motion given on the left. Bottom: absolute difference between induced and estimated motion fields.

of 641 × 670 pixels while using only a single core of 12 core processor at 2.6 GHz. For this given setup, *rigid* registration and motion correction took 42 iterations and approximately 10 s. The second fastest method was the *affine* registration, which took 47 iterations and approximately 15 s. *Nonrigid* registration with an optimized $C_{\text{regularization}}(T) = 2 \times 10^{-4}$ was the slowest method, which took 201 iterations and approximately 90 s. *Two-stage* registration with an optimized $C_{\text{regularization}}(T) = 3 \times 10^{-2}$ took 47 iterations for *affine* and eight iterations for *nonrigid* registration with a total of 20 s approximately.

B. Simulation Results for the Realistic Motion

A B-mode image with motion was generated with 20-dB SNR using the motion field extracted from the clinical scan shown in Fig. 4 (middle). This frame with motion was registered to a reference B-mode image without motion by using *nonrigid*, *affine*, and *two-stage* motion estimation methods. Fig. 7 (top) shows the motion field estimated by different methods and Fig. 7 (bottom) shows the absolute difference between induced and estimated motion fields. Amongst all the methods presented, the *two-stage* method has the lowest mean absolute error value of 12.2 μm, which increased to 15.3 μm for the *nonrigid* method and 28.7 μm for the *affine* method. When using the *two-stage* method, the absolute motion estimation error was less than 15 μm for 70% of the total image area, whereas this area drops down to 65% for the *nonrigid* and 38% for the *affine* method.

Overall, the *rigid* method has the worst performance since it cannot accommodate the localized shearing and rotation of the tissue for this case of simulated realistic motion. The *affine*

method has good performance for this case; however, it performs worse than the *two-stage* method. The second *nonrigid* registration stage of the *two-stage* method compensates for the local deformations and gives an advantage over the *affine* method. The *nonrigid* method works best for small local deformations, however, when the motion is larger than a few pixels the performance drops significantly, which is visible in the south–west corner of Fig. 7 (bottom–middle). Therefore, the *two-stage* method is a good composite method that compensates the large global motion first and provides a better starting point for the *nonrigid* registration stage.

C. Effect of Regularization Parameter

By comparing the computation time, it is easy to notice the advantage of the *two-stage* registration against *nonrigid* registration. According to the previously given example, *nonrigid* registration with an optimized regularization parameter performed 201 iterations, where the *two-stage* registration with an optimized regularization parameter performed a total of 55 iterations to minimize the cost function. The first stage compensates a large portion of the motion by using the faster *affine* method and requires fewer iterations for the slower second stage based on the *nonrigid* registration.

Although speed improvement is a big advantage when using the *two-stage* method, the most important benefit of this method is improved estimation robustness when using a nonoptimized regularization parameter. To demonstrate this, a large image region (between 10 to 35 mm in depth and between -13 to 13 mm in lateral) and a smaller region (between 10 to 30 mm in depth and between -8 to 13 mm in lateral) were chosen from the same data set simulated with the realistic motion, where the small region avoids the large motion at the south–west corner of Fig. 4 (middle).

Performance of all estimation methods for this simulation is shown in Fig. 8 (top) for the small region and (bottom) the large region. The mean absolute error values calculated for each method is plotted against the regularization parameter. *Rigid* and *affine* registration methods do not use a regularization parameter, so they have the same constant value for the whole range. The performance of the *nonrigid* and the *two-stage* registration methods depends on the regularization parameter, where the performance is best for the optimized values highlighted by red and blue circles in Fig. 8.

For the small region, the *rigid* method has the largest error between all methods due to the shearing and rotation of the tissue. When the regularization parameter is optimized, the *nonrigid* and the *two-stage* methods have similar error values. However, the *two-stage* method provides a better performance for a broader range of regularization parameters, which is advantageous for real-time applications where the optimization of the regularization parameter may not be possible for every frame.

For the large region, the *rigid* method again has the largest error as shown in Fig. 8 (bottom). The *affine* and the *two-stage* methods performed similarly for both the large and small regions, but the performance of the *nonrigid* method dropped significantly. By comparing the results after choosing a large and a small area from the same B-mode image, one can conclude that the robustness of the *two-stage* motion estimation method is better than the *nonrigid* method.

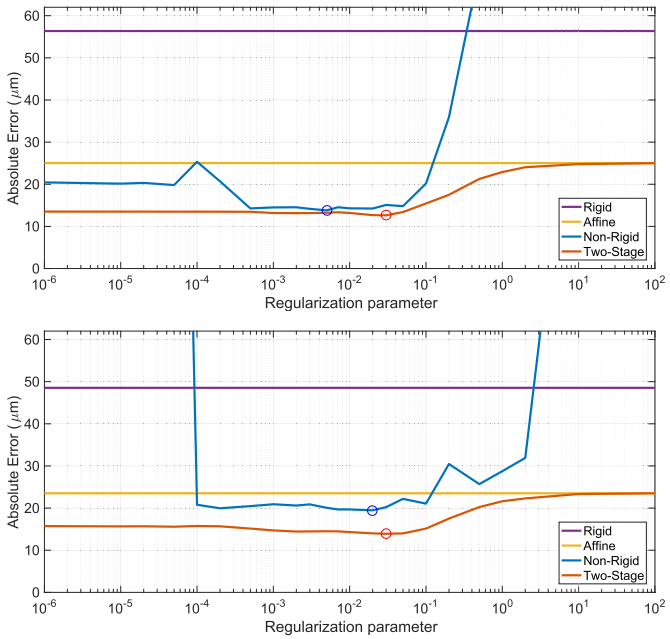

Fig. 8. Performance of *nonrigid* and *two-stage* methods are demonstrated with a varying regularization parameters. Top: small region of interest. Bottom: large region of interest. *Rigid* and *affine* methods are not regularized, so they always estimate the same motion field for a given image.

D. Clinical Results

It is hard to demonstrate the accuracy of the motion estimation and correction on the clinical data set without knowing the ground truth. Therefore, this section demonstrates the use of the *two-stage* motion estimation on clinical SR images based on the assumption that healthy volunteers without peripheral arterial disease should have long straight vascular structures without stenosis and tortuous vessels, as demonstrated by [32] and [33] using angiograms and micrographs.

Fig. 9 shows the CEUS maximum intensity projection (MIP) and the SR image generated from a 45-s clinical scan with 580 frames. Using less than a minute of clinical data acquisition, the imaging region was visualized using the SR method with an average number of localizations of 30 MBs/frame. Motion correction was performed by using the estimated motion with the *two-stage* method, where the estimated motion from two selected regions are shown in Fig. 9 (bottom) as a demonstration. An average motion of 233 ± 17 μm/s was estimated from the clinical US scans. Qualitatively, it is clear that the spatial resolution of the SR image is higher than that of the MIP.

Fig. 10 (top) demonstrates the effect of motion correction on a chosen vessel. The average thickness of the vessel inside the boxes are given in Fig. 10 (bottom). The sizes of the vessels from these images were measured by using linear interpolation [34]. The full width at half maximum (FWHM) of the vessel was measured as 1075 μm from the MIP image without

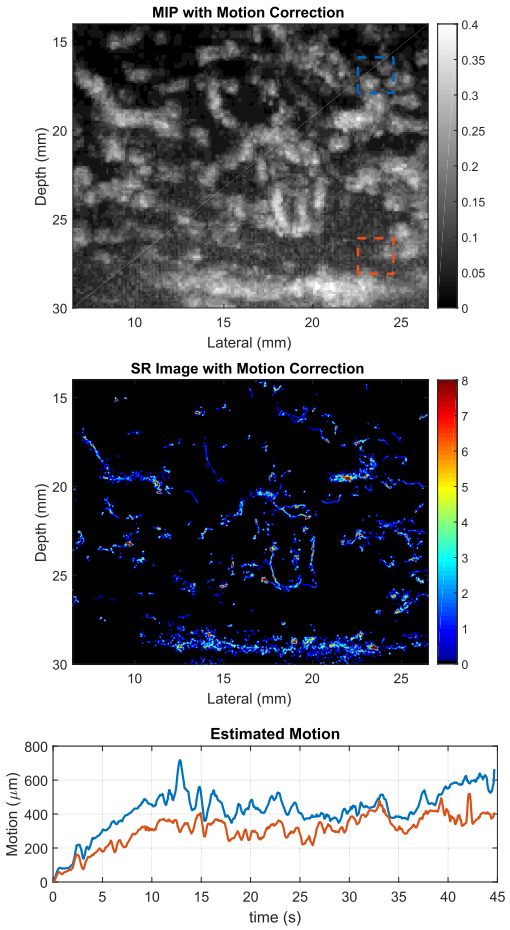

Fig. 9. Top: MIP of the CEUS frames acquired from healthy human volunteers. Middle: SR image created using the same CEUS frames after motion correction. Colorbar corresponds to the number of localized MBs. Bottom: estimated motion from the clinical data is plotted for the red and blue rectangles shown in the MIP image as a function of time.

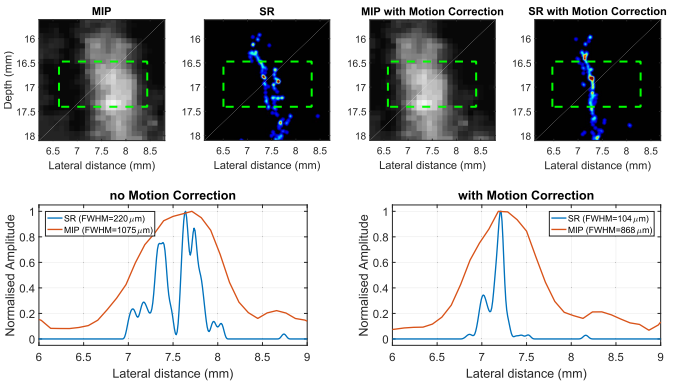

Fig. 10. Top: CEUS MIP and SR image of a selected vessel is shown with and without motion correction. Bottom: average thickness of the vessel inside the green boxes are plotted to demonstrate the achieved improvement after motion correction.

motion correction. The SR image without motion correction achieved a subwavelength vessel FWHM of 220 μm; however, after the application of proposed *two-stage* motion correction method, the FWHM of the vessel was reduced to 104 μm and the double-vessel feature disappeared.

The benefit of using *two-stage* motion estimation and motion correction on SR imaging in human microvasculature is demonstrated in Fig. 11. The microvessels were chosen from four different SR images acquired from three healthy volunteers. Fig. 11 shows the effect of the proposed *two-stage* motion correction on different microvessels, where the thickness of vessels are given in Table I. After motion correction the torturous vessels appeared as straight vessels, which shows the significance of the *two-stage* motion correction on clinical interpretation of SR US images. Motion correction also potentially removed blurred vessels and artificial double copies, which were mostly visualized as single vessels after correction. After motion correction, the size of the average vessel in the SR image dropped from 146 μm down to 94 μm by reducing the width of the motion-blurred microvessels approximately 1.5-fold as listed in Table I.

V. Discussion

Motion is an inherent part of *in vivo* imaging and US imaging methods based on multiple acquisitions suffer from motion artifacts even for images acquired at high frame rates with or without MBs [35]–[37]. For SR imaging, subwavelength motion correction methods are required to visualize microvascular structures and flow beyond the diffraction limit through localization of spatially isolated MBs. Rigid motion estimation techniques using image data cannot compensate for local deformations as demonstrated in the simulation study presented here.

This paper employed an image-based motion estimation approach for SR US imaging. The applied *two-stage* method is a combination of *affine* image registration that can estimate the global motion, and *nonrigid* image registration that can estimate the local deformation of tissue. The main advantage of using a two-stage registration instead of a *nonrigid* registration is that the *nonrigid* method is more complex and computationally heavy. The first stage, *affine* registration, compensates for the global motion and it gives a better starting point for the *nonrigid* stage, which also reduces the number of iterations required to minimize the cost function.

For the first two simulation studies with the probe motion and tissue deformations, presented in Figs. 5 and 6, the standard deviation values are relatively large since the displayed results present a combination of many simulations performed for 11 different motion amplitudes between 1 and 1024 μm. For the same simulations, the accuracy of the motion estimation was better in the axial direction for all methods due to the shape of the point spread function, which was narrower in the axial direction. These two sets of simulations were performed to assess the feasibility of the motion estimation methods; however, the motion field was too simplistic to highlight the advantages of the *two-stage* registration method compared with *affine* registration. The *affine* method has the degrees of freedom required to correct for the simplistic motion, whereas the *two-stage* method has many more degrees of freedom. For these simulations, the proposed *two-stage* method achieved similar results with the *affine* method with a mean absolute motion estimation error of 7.5 $\pm$ 5.8 μm or less for the

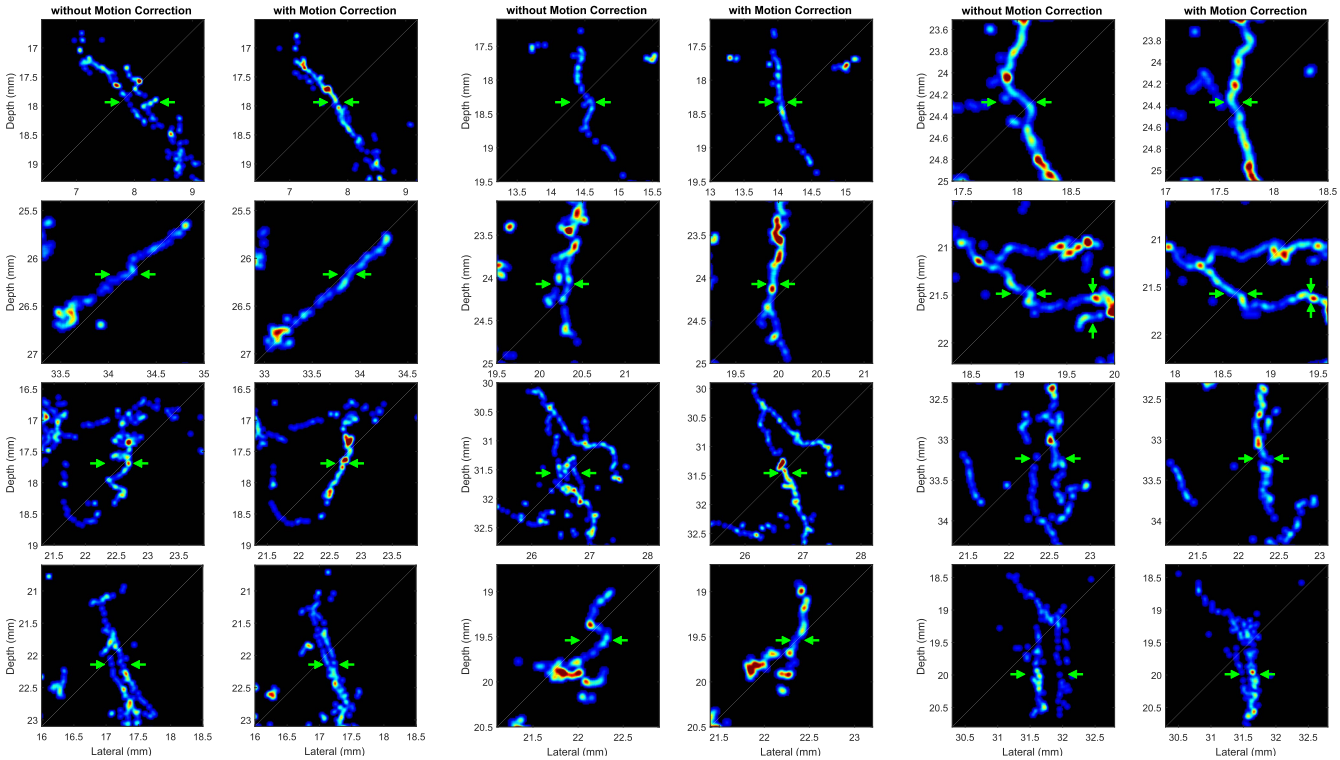

Fig. 11. Effect of motion correction is presented in 12 SR image pairs. Images are displayed in three columns. Left: image is without motion correction. Right: image is with motion correction. Colorbar is the same as Fig. 9 and it corresponds to the number of localized MBs.

TABLE I
MICROVESSEL THICKNESS (MICROMETERS)

Method	MV 1	MV 2	MV 3	MV 4	MV 5	MV 6	MV 7	MV 8	MV 9	MV 10	MV 11	MV 12	ALL
MIP	1075	688	1786	2433	1839	1347	788	1878	2080	2172	1746	1429	1605±548
SR	220	170	86	155	163	122	191	258	92	100	85	104	146±57
MIP w/ MC	868	623	1229	911	766	1386	684	1834	2219	1640	1291	1232	1224±491
SR w/ MC	104	72	78	71	104	74	99	116	97	108	89	121	94±17

simulated motion range of 1–1024 μm with 20-dB SNR. However, for the simulation with realistic motion field, the advantage of using the *two-stage* method over *affine* method became obvious, where the mean absolute error was 2.3 times smaller for the *two-stage* method.

The error values presented in this paper will change as a function of many variables such as wavelength, sampling frequency, imaging resolution, SNR, and regularization parameter. Improving some of these parameters and also using RF data instead of image data can increase the estimation accuracy. Although, in this paper, the motion estimation was performed on B-mode images acquired by a commercial scanner, the application of the proposed motion correction scheme to RF data is possible [38]. Using RF data instead of image data can increase the estimation accuracy, as the RF domain is a superset of the image domain with an additional signal phase information.

The regularization penalty might have a significant impact on the motion estimation error for the *nonrigid* method; however, it is possible to achieve a reasonable estimation accuracy for a large range of regularization values while using the *two-stage* method as shown in Fig. 8. For both the simulation and clinical US data used in this paper, the smallest used value was $C_{\text{regularization}}(T) = 2 \times 10^{-4}$. Below this value, the computation time of the estimation process increases without a benefit since a lower penalty results in a viscouslike registration, which is not realistic for human soft tissue. Above the largest used value of $C_{\text{regularization}}(T) = 0.5$, estimation results in an affinelike registration, which is not suitable for estimating complex nonrigid motion fields.

The motion estimation can be performed using either a dynamic or a static reference frame. It is possible to perform registration between each pair of consecutive frames by changing the reference frame for every registration; however, this results in an accumulation of error over every registered frame. In this paper, motion estimation was performed by using a single reference frame. In this case, the choice of the reference frame becomes crucial. If the specific chosen reference frame is corrupted with artifacts or significant motion, this can make it very different from the rest of the frames in the sequence. An automatic and systematic way of choosing a good quality reference frame may eliminate this problem.

Future improvement can include groupwise registration of the entire video sequence together rather than pairwise registration [39].

There are two significant limitations in SR US imaging performed in 2-D. The biggest problem is the out-of-plane motion that cannot be compensated using 2-D imaging methods. Before starting the motion correction procedure for the clinical study, the B-mode and CEUS frames were visually inspected. Video files were segmented into smaller sections with no obvious out-of-plane motion in the B-mode images. From these segmented videos, only those with 250 or more frames were selected for further processing. Out of 5–7 min of US and CEUS acquisitions from three volunteers, only four continuous acquisitions with a duration of 40–55 s were suitable for SR imaging after motion correction. The tibialis anterior muscle is located at one of the extremities of human body and is, therefore, not affected by respiration and cardiac motion. When imaging in the abdomen and chest region, while the motion correction algorithm was designed to cope with large motion amplitude including that expected in abdomen, increased out-of-plane motion will limit the applicability of our approach in its 2-D form, as the current correction procedure relies on a constant 2-D plane in the sample being imaged over time. In the future, it should be possible to apply our approach when imaging in the liver, pancreas or kidney using a 3-D imaging approach, or 2-D SR US provided that an experienced clinician places the probe in a way that the imaging region only moves in-plane with the probe. Second, the acquired SR images did not have the required resolution in the elevation direction. Both of these issues can be addressed by using 3-D imaging methods, which can achieve the required elevational resolution and SNR for 3-D SR imaging [40]–[42]. Although 3-D imaging offers a solution to the problem of out-of-plane motion, it may introduce other limitations for SR US imaging. For multiplexed 3-D US systems, the acquired volume data is a combination of multiple transmissions and acquisitions, which may generate intravolume motion artifacts. High frame rate 3-D US imaging with plane waves is capable of imaging the whole volume with a single acquisition. However, this method suffers from low SNR due to the lack of elevational focusing, which may increase the localization error in SR US imaging. A carefully chosen imaging strategy is required for the 3-D SR US to balance the tradeoffs between motion artifacts and localization error. High speed implementation of 3-D SR remains a big challenge due to postprocessing complexity and data size for both multiplexed and plane wave 3-D US imaging.

The SR images shown in Fig. 11 have all been selected using visually perceived improvement in image quality, based on an assumption that the microvessels should be long and straight in healthy patients [32], [33]. It is not possible to calculate the resolution of the SR images due to the lack of the ground truth. Nevertheless, it is possible to measure the width of the microvessels, where the motion corrected SR imaging method will not give an underestimate of the width due to motion and localization error. For this reason, the spatial resolution of the SR images generated in this paper using a clinical US system has to be <94 μm ($\lambda \approx 250$ μm), and therefore, these results represent the first clinical localization-based SR US imaging.

This paper used a data set acquired by a clinical scanner with normal frame-rate and demonstrated the use of a motion correction method without considering the computational speed. The motion estimation and correction were performed by using a MATLAB code and executed on a CPU; however, it is possible to significantly improve the computational time of the applied method by using a GPU or other parallel processing approaches. A fast motion correction can empower the image-based superlocalization technique and lead to quick clinical translation of SR US imaging.

VI. Conclusion

Clinical motion observed in US imaging is an aggregation of various motion types. Probe movement, respiration, cardiac motion, and many other unavoidable sources of body motion result in a combination of translation, shearing, and nonrigid deformations at different scales. SR images are generated through multiple US frames acquired over a duration of seconds to minutes, where both large tissue movements and small local deformations can be observed. To estimate both large- and small-scale motion and local deformations simultaneously with high precision, this paper used a *two-stage* approach for US SR imaging.

Ideally, SR US imaging should be limited by the localization precision rather than sample motion. Therefore, motion should be compensated with an accuracy higher than the spatial resolution of the SR image as demonstrated in this paper. The feasibility study showed that it was possible to achieve a subpixel ($x = 60$ μm) and subwavelength ($\lambda \approx 250$ μm) motion estimation accuracy of 7.5 ± 5.8 μm or better for the simulated probe motion and tissue deformations while using the *two-stage* image registration method. Similar results were achieved for the simulations with a realistic motion extracted from a clinical data set, where the mean absolute error was 12.2 μm and 70% of the motion was estimated with an absolute error smaller than 15 μm. The *two-stage* method was then applied to achieve clinical SR US imaging of microvasculature in human lower limb using a commercially available clinical US scanner.

References

[1] O. Couture, B. Besson, G. Montaldo, M. Fink, and M. Tanter, "Microbubble ultrasound super-localization imaging (MUSLI)," in *Proc. IEEE Int. Ultrason. Symp. (IUS)*, Oct. 2011, pp. 1285–1287.

[2] O. M. Viessmann, R. J. Eckersley, K. Christensen-Jeffries, M. X. Tang, and C. Dunsby, "Acoustic super-resolution with ultrasound and microbubbles," *Phys. Med. Biol.*, vol. 58, no. 18, pp. 6447–6458, Sep. 2013.

[3] Y. Desailly, O. Couture, M. Fink, and M. Tanter, "Sono-activated ultrasound localization microscopy," *Appl. Phys. Lett.*, vol. 103, no. 17, p. 174107, 2013.

[4] M. A. O'Reilly and K. Hynynen, "A super-resolution ultrasound method for brain vascular mapping," *Med. Phys.*, vol. 40, no. 11, p. 110701, Nov. 2013.

[5] K. Christensen-Jeffries, R. J. Browning, M.-X. Tang, C. Dunsby, and R. J. Eckersley, "*In vivo* acoustic super-resolution and super-resolved velocity mapping using microbubbles," *IEEE Trans. Med. Imag.*, vol. 34, no. 2, pp. 433–440, Feb. 2015.

[6] C. Errico *et al.*, "Ultrafast ultrasound localization microscopy for deep super-resolution vascular imaging," *Nature*, vol. 527, pp. 499–507, Nov. 2015.

[7] D. Ackermann, G. Schmitz, and S. Member, "Detection and tracking of multiple microbubbles in ultrasound B-mode images," *IEEE Trans. Ultrason., Ferroelect., Freq. Control*, vol. 63, no. 1, pp. 72–82, Jan. 2016.
[8] F. Lin, S. E. Shelton, D. Espíndola, J. D. Rojas, G. Pinton, and P. A. Dayton, "3-D ultrasound localization microscopy for identifying microvascular morphology features of tumor angiogenesis at a resolution beyond the diffraction limit of conventional ultrasound," *Theranostics*, vol. 7, no. 1, pp. 196–204, 2017.
[9] A. Bar-Zion, C. Tremblay-Darveau, O. Solomon, D. Adam, and Y. C. Eldar, "Fast vascular ultrasound imaging with enhanced spatial resolution and background rejection," *IEEE Trans. Med. Imag.*, vol. 36, no. 1, pp. 169–180, Jan. 2017.
[10] Y. Desailly, J. Pierre, O. Couture, and M. Tanter, "Resolution limits of ultrafast ultrasound localization microscopy," *Phys. Med. Biol.*, vol. 60, no. 22, pp. 8723–8740, Nov. 2015.
[11] V. Hingot, C. Errico, M. Tanter, and O. Couture, "Subwavelength motion-correction for ultrafast ultrasound localization microscopy," *Ultrasonics*, vol. 77, pp. 17–21, May 2017.
[12] C. Catana, "Motion correction options in PET/MRI," *Seminars Nucl. Med.*, vol. 45, no. 3, pp. 212–223, 2015.
[13] E. J. Chen, J. Novakofski, W. K. Jenkins, and W. O'Brien, "Young's modulus measurements of soft tissues with application to elasticity imaging," *IEEE Trans. Ultrason., Ferroelect., Freq. Control*, vol. 43, no. 1, pp. 191–194, Jan. 1996.
[14] J. Porée, D. Posada, A. Hodzic, F. Tournoux, G. Cloutier, and D. Garcia, "High-frame-rate echocardiography using coherent compounding with Doppler-based motion-compensation," *IEEE Trans. Med. Imag.*, vol. 35, no. 7, pp. 1647–1657, Jul. 2016.
[15] K. L. Gammelmark and J. A. Jensen, "2-D tissue motion compensation of synthetic transmit aperture images," *IEEE Trans. Ultrason., Ferroelectr., Freq. Control*, vol. 61, no. 4, pp. 594–610, Apr. 2014.
[16] N. Sheikov, N. McDannold, N. Vykhodtseva, F. Jolesz, and K. Hynynen, "Cellular mechanisms of the blood-brain barrier opening induced by ultrasound in presence of microbubbles," *Ultrasound Med. Biol.*, vol. 30, no. 7, pp. 979–989, 2007.
[17] S. E. Shelton *et al.*, "Quantification of microvascular tortuosity during tumor evolution using acoustic angiography," *Ultrasound Med. Biol.*, vol. 41, no. 7, pp. 1896–1904, Jul. 2015.
[18] Y. Yokoi, *Basics of Angiography for Peripheral Artery Disease* (Angiography and Endovascular Therapy for Peripheral Artery Disease). Rijeka, Croatia: InTech, 2017, pp. 1–37.
[19] S. Harput *et al.*, "Two stage sub-wavelength motion correction in human microvasculature for CEUS imaging," in *Proc. IEEE Int. Ultrason. Symp. (IUS)*, Sep. 2017, pp. 1–4.
[20] K. Christensen-Jeffries, "Super-resolution ultrasound imaging with microbubbles," Ph.D. dissertation, Division Imag. Sci. Biomed. Eng., School Med., King's College London, London, U.K., 2016.
[21] D.-J. Kroon. *B-Spline Grid, Image and Point Based Registration*. Accessed: Jan. 2017. [Online]. Available: https://uk.mathworks.com/matlabcentral/fileexchange/20057-b-spline-grid–image-and-point-based-registration
[22] D. Rueckert, L. I. Sonoda, C. Hayes, D. L. G. Hill, M. O. Leach, and D. J. Hawkes, "Nonrigid registration using free-form deformations: Application to breast MR images," *IEEE Trans. Med. Imag.*, vol. 18, no. 8, pp. 712–721, Aug. 1999.
[23] S. Lee, G. Wolberg, and S. Y. Shin, "Scattered data interpolation with multilevel B-splines," *IEEE Trans. Vis. Comput. Graphics*, vol. 3, no. 3, pp. 228–244, Jul./Sep. 1997.
[24] C. Demené *et al.*, "Spatiotemporal clutter filtering of ultrafast ultrasound data highly increases Doppler and fUltrasound sensitivity," *IEEE Trans. Med. Imag.*, vol. 34, no. 11, pp. 2271–2285, Nov. 2015.
[25] M.-X. Tang and R. J. Eckersley, "Nonlinear propagation of ultrasound through microbubble contrast agents and implications for imaging," *IEEE Trans. Ultrason., Ferroelect., Freq. Control*, vol. 53, no. 12, pp. 2406–2415, Dec. 2006.
[26] J. Brown, K. Christensen-Jeffries, S. Harput, C. Dunsby, M. X. Tang, and R. J. Eckersley, "Investigation of microbubble detection methods for super-resolution imaging of microvasculature," in *Proc. IEEE Int. Ultrason. Symp. (IUS)*, Sep. 2017, pp. 1–4.
[27] K. Christensen-Jeffries *et al.*, "Microbubble axial localization errors in ultrasound super-resolution imaging," *IEEE Trans. Ultrason., Ferroelect., Freq. Control*, vol. 64, no. 11, pp. 1644–1654, Nov. 2017.
[28] J. A. Jensen and N. B. Svendsen, "Calculation of pressure fields from arbitrarily shaped, apodized, and excited ultrasound transducers," *IEEE Trans. Ultrason., Ferroelect., Freq. Control*, vol. 39, no. 2, pp. 262–267, Mar. 1992.
[29] J. A. Jensen, "FIELD: A program for simulating ultrasound systems," in *Proc. IEEE 10th Nordic-Baltic Conf. Biomed. Imag.*, vol. 34. Mar. 1996, pp. 351–353.
[30] J. M. Thijssen, "Ultrasonic speckle formation, analysis and processing applied to tissue characterization," *Pattern Recognit. Lett.*, vol. 24, nos. 4–5, pp. 659–675, Feb. 2003.
[31] Z. Zhang and C. F. Martin, "Convergence and Gibbs' phenomenon in cubic spline interpolation of discontinuous functions," *J. Comput. Appl. Math.*, vol. 87, no. 2, pp. 359–371, 1997.
[32] F. Bosetti *et al.*, "'Small blood vessels: Big health problems?': Scientific recommendations of the national institutes of health workshop," *J. Amer. Heart Assoc.*, vol. 5, no. 11, p. e004389, 2016.
[33] H.-C. Han, "Twisted blood vessels: Symptoms, etiology and biomechanical mechanisms," *J. Vascular Res.*, vol. 49, no. 3, pp. 185–197, 2012.
[34] S. Harput, J. McLaughlan, D. M. J. Cowell, and S. Freear, "New performance metrics for ultrasound pulse compression systems," in *Proc. IEEE Int. Ultrason. Symp. (IUS)*, Sep. 2014, pp. 440–443.
[35] J. Wang and J.-Y. Lu, "Motion artifacts of extended high frame rate imaging," *IEEE Trans. Ultrason., Ferroelect., Freq. Control*, vol. 54, no. 7, pp. 1303–1315, Jul. 2007.
[36] J. Viti, H. J. Vos, N. de Jong, F. Guidi, and P. Tortoli, "Detection of contrast agents: Plane wave versus focused transmission," *IEEE Trans. Ultrason., Ferroelect., Freq. Control*, vol. 63, no. 2, pp. 203–211, Feb. 2016.
[37] C. H. Leow and M.-X. Tang, "Spatio-temporal flow and wall shear stress mapping based on incoherent ensemble-correlation of ultrafast contrast enhanced ultrasound images," *Ultrasound Med. Biol.*, vol. 44, no. 1, pp. 134–152, 2018.
[38] M. Toulemonde *et al.*, "Effects of motion on high frame rate contrast enhanced echocardiography and its correction," in *Proc. IEEE Int. Ultrason. Symp. (IUS)*, Sep. 2017, pp. 1–4.
[39] C. T. Metz, S. Klein, M. Schaap, T. van Walsum, and W. J. Niessen, "Nonrigid registration of dynamic medical imaging data using nD + t B-splines and a groupwise optimization approach," *Med. Image Anal.*, vol. 15, no. 2, pp. 238–249, 2011.
[40] A. Ramalli, E. Boni, A. S. Savoia, and P. Tortoli, "Density-tapered spiral arrays for ultrasound 3-D imaging," *IEEE Trans. Ultrason., Ferroelect., Freq. Control*, vol. 62, no. 8, pp. 1580–1588, Aug. 2015.
[41] K. Christensen-Jeffries, J. Brown, P. Aljabar, M. Tang, C. Dunsby, and R. J. Eckersley, "3-D *in vitro* acoustic super-resolution and super-resolved velocity mapping using microbubbles," *IEEE Trans. Ultrason., Ferroelect., Freq. Control*, vol. 64, no. 10, pp. 1478–1486, Oct. 2017.
[42] E. Roux, A. Ramalli, H. Liebgott, C. Cachard, M. C. Robini, and P. Tortoli, "Wideband 2-D array design optimization with fabrication constraints for 3-D US imaging," *IEEE Trans. Ultrason., Ferroelect., Freq. Control*, vol. 64, no. 1, pp. 108–125, Jan. 2017.

Sevan Harput received the B.Sc. degree in microelectronics engineering and the M.Sc. degree in electronic engineering and computer sciences from Sabanci University, Istanbul, Turkey, in 2005 and 2007, respectively, and the Ph.D. degree from University of Leeds, Leeds, U.K., in 2013.

He is currently a Research Associate with the Department of Bioengineering, Imperial College London, London, U.K., and a Visiting Scholar with King's College London, London, and the University of Leeds. His research interests include high frame-rate ultrasound imaging, super-resolution imaging, ultrasound contrast agents, signal processing for biomedical imaging, nonlinear acoustics, ultrasound sensor modeling, and biomedical device development.

Dr. Harput has been an Editorial and Administrative Assistant with the IEEE TRANSACTIONS ON ULTRASONICS, FERROELECTRICS, AND FREQUENCY CONTROL since 2013.

Kirsten Christensen-Jeffries received the B.Sc. degree in maths and physics from the University of Warwick, Coventry, U.K., in 2010, and the M.Res. degree in biomedical imaging with Imperial College London, London, U.K., in 2011.

She spent eight months working with IXICO, London, in 2011/2012. She currently holds a post-doctoral research position at the Ultrasound Imaging Group, Kings College London, London. Her research interests include contrast enhanced ultrasound imaging, with a focus on the development of super-resolution ultrasound imaging techniques for visualisation of the microvasculature.

Jemma Brown received the M.Phys. degree from the University of Oxford, Oxford, U.K., in 2015. She is currently pursuing the Ph.D. degree in medical imaging with the ESPRC Centre, Kings College London, and Imperial College London, London, U.K., with a focus on super-resolution ultrasound, under the supervision of Dr. Eckersley and Dr. Tang.

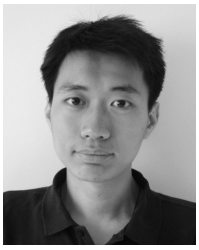

Yuanwei Li received the B.Eng. degree in bioengineering from Imperial College London, London, U.K., in 2012, the M.Sc. degree in computer science from the University of Oxford, Oxford, U.K., in 2013, and the Ph.D. degree from Imperial College London, in 2017.

He is currently a Post-Doctoral Researcher with the BioMedIA Group, Imperial College London. His research interests include medical image analysis using machine learning.

Katherine J. Williams is currently an Honorary Clinical Research Fellow with the Faculty of Medicine, Department of Surgery and Cancer, Imperial College London, London, U.K. She is running clinical trials on evaluation of musculoskeletal microcirculation with ultrasound, neuromuscular electrical stimulation (NMES) in the management of diabetic foot ulcers, nerves, peripheral arterial disease, venous Insufficiency, and neuromuscular stimulation. Her research interests include NMES of the lower limb.

Alun H. Davies received the M.A., D.M., and D.Sc. degrees from the University of Cambridge, Cambridge, U.K.

He is currently a Professor of vascular surgery with Imperial College London, London, U.K., and a Consultant Surgeon whose NHS practice is based at Charing Cross Hospital, London, and St. Mary's Hospital, London. He trained in Cambridge, Oxford, Plymouth, Boston, USA, and Bristol. In 1994, he joined Charing Cross Hospital, where he held a consultant appointment. He is regarded as a world expert in the management of venous disorder. He has written extensively on many aspects of vascular disease, writing over 440 peer-reviewed manuscripts, presents regularly at international meetings, and runs a large research group. He is currently the Chief Investigator of three NIHR funded trials.

Dr. Davies is a member of the American Venous Forum, the Vascular Surgical Society of Great Britain and Ireland, and the European Society of Vascular Surgery, and a fellow of RCS, HEA, the American College of Phlebology, and EBVS. He has been a Hunterian Professor at the RCS, U.K., and is an Emeritius Fellow of the Australasian College of Phlebology. He was the Chairman of the Varicose Vein Guideline Group for the National Institute of Clinical Excellence (NICE) and a member of the Quality Standards Group, the NICE Guidelines Group on AAA, and the national CRG for vascular surgery. He is also the Director of the European College of Phlebology and has Co-Chaired the ESVS Guidelines Group on the management of varicose veins. He is Editor-in-Chief of *Phlebology*, a past President of the European Venous Forum and The Venous Forum at The Royal Society of Medicine, and the Treasurer of the Surgical and Academic Research Society.

Robert J. Eckersley received the B.Sc. degree in physics from the King's College London, London, U.K., in 1991, and the Ph.D. degree from the Institute of Cancer Research, Royal Marsden Hospital, University of London, London, in 1997.

He was with the Hammersmith Hospital NHS Trust, London, and in 1999 was awarded an MRC Research Training Fellowship. As part of this fellowship, he spent some time at the Sunnybrook Health Sciences Centre, University of Toronto. He subsequently continued as a Post-Doctoral Researcher within the Imaging Sciences Department, Imperial College London, London, and became a Nonclinical Lecturer in ultrasound in 2007. In 2012, he joined the Biomedical Engineering Department, King's College London, as a Senior Lecturer. His research interests range from fundamental studies to clinical applications. Examples include image and signal analysis of ultrasound data for functional imaging or tissue characterization, nonlinear imaging for improved detection of microbubbles, and understanding errors and artifacts in ultrasound contrast imaging.

Christopher Dunsby received the M.S. degree from the University of Bristol, Bristol, U.K., in 2000, and the Ph.D. degree from Imperial College London, London, U.K., in 2003.

He is currently a Reader with a joint post between Photonics, Department of Physics, and the Centre for Pathology, Department of Medicine, Imperial College London. His research interests include the application of photonics and ultrafast laser technology to biomedical imaging, multiphoton microscopy, multiparameter fluorescence imaging and fluorescence lifetime imaging, and methods for super-resolution ultrasound imaging.

Meng-Xing Tang held a post-doctoral position at the Department of Engineering Science, University of Oxford, Oxford, U.K. He joined the Department of Bioengineering, Imperial College London, London, U.K., as a Lecturer (Assistant Professor) in 2006. He was promoted to a Senior Lecturer (Associate Professor) in 2011 and a Reader in biomedical imaging in 2015. He founded and is currently leading the Ultrasound Laboratory for Imaging and Sensing (previously the Ultrasound Imaging Group). He has authored over 70 peer-reviewed journal papers. His current research focuses on developing new imaging and image analysis techniques using ultrasound and its allied techniques, such as microbubble contrast agents (MBs), for quantifying physiological flow, tissue perfusion, and molecular information, and their applications in cardiovascular diseases, cancer, and neurology. In the past years, his group has investigated extensively the imaging physics of MBs, the various imaging artifacts in CEUS and their correction methods, in order to achieve more reliable quantification of tissue perfusion. More recently his group has been developing and applying new contrast-enhanced ultrasound imaging techniques of very high temporal and spatial resolution and image contrast. His research has been generously funded by U.K. EPSRC, Cancer Research U.K., the British Heart Foundation, the Wellcome Trust, and the Royal Society.

Dr. Tang is an Associate Editor of the IEEE TRANSACTIONS ON ULTRASONICS, FERROELECTRICS, AND FREQUENCY CONTROL, and is on the Editorial Advisory Board of *Ultrasound in Medicine and Biology*.